Magnetic Resonance in Medicine 47:888–895 (2002)
DOI 10.1002/mrm.10145

Respiration-Induced B_0 Fluctuations and Their Spatial Distribution in the Human Brain at 7 Tesla

Pierre-François Van de Moortele,[1*] Josef Pfeuffer,[1] Gary H. Glover,[2] Kamil Ugurbil,[1] and Xiaoping Hu[1]

In functional magnetic resonance imaging (fMRI), it is known that physiological influences such as cardiac pulsation, respiration, and brain motion can induce fluctuations in signal intensity and phase. Some of the mechanisms potentially involved in those phenomena are expected to be amplified at higher magnetic fields. This study addresses the issue of B_0 fluctuations induced by susceptibility changes during respiration attributed to movements of chest and diaphragm, and variations in the oxygen concentration. It is demonstrated that respiration-induced resonance offsets (RIROs) are significant at 7T. Data were acquired with an RF pulse (no gradients), multislice echo-planar imaging (EPI), and dynamic 3D fast low-angle shot (3D-FLASH) imaging. Three main observations summarize the experimental findings. First, in FIDs measured after a single RF pulse, a RIRO with a large amplitude was consistently detected, although the average amplitude varied between subjects from 1.45 Hz to 4 Hz. Second, in transverse EPI images obtained in the occipital lobe, the RIRO amplitude showed a monotonic increase along the *z* axis toward the lungs. Third, a more detailed spatial analysis with 3D-FLASH phase maps revealed that a previously published analytical model can accurately describe the spatial distribution of RIRO. Consequential apparent motions in the EPI series, as well as the implications of slice orientation for correction strategies are discussed. Magn Reson Med 47:888–895, 2002. © 2002 Wiley-Liss, Inc.

Key words: physiological artifacts; respiration artifacts; echo-planar imaging; B_0 fluctuation; off-resonance

Ultra-high-field human MR scanners (>4T) provide advantages both for functional MRI (fMRI) of the brain and for MR spectroscopy (MRS) (1–4) because of their increased signal-to-noise ratio (SNR), better spectral resolution in metabolite studies, and increased sensitivity and specificity in blood oxygenation level-dependent (BOLD) fMRI. However, higher magnetic fields induce higher susceptibility-related magnetic field alterations, leading to potential shimming problems due to the static components of the B_0 inhomogeneities. In addition, fluctuations of B_0 with time, related to the displacement in space of structures with different magnetic susceptibilities and/or to susceptibility changes, are expected to increase at higher magnetic fields. This work investigates global respiration-induced resonance offsets (RIROs) in the brain at 7T, taking into account the following observations:

1. It has been shown that physiological processes, such as respiration and cardiovascular pulsation, induce significant fluctuations in fMRI data (5–17).
2. It has been suggested that, in addition to brain motion, blood pulsation, and/or cerebrospinal fluid (CSF) movement, susceptibility changes due to motion of the lungs, diaphragm, and chest during breathing, as well as changes in gas susceptibility could be responsible for signal fluctuations in the brain by means of a B_0 modulation (8,10,12,18). For example, at 3T a respiration-induced B_0 modulation of about 0.01 ppm (i.e., about 1.25 Hz) was reported in the human brain (12,19).
3. Echo planar imaging (EPI), a fast-imaging sequence widely used in fMRI studies, is highly sensitive to off-resonance effects because of its low sampling bandwidth along the phase-encoding direction (18,20–22). The consequences of B_0 fluctuations in EPI series have been previously discussed for a variety of sources, including eddy currents (21), long-term B_0 drift (23), and external magnetic field perturbation (22). Raj et al. (18) proposed and tested a model, using a phantom, which showed that susceptibility variations generated during respiration are expected to be responsible for apparent motion, distortion, and intensity profile alterations in EPI images. Recently, the same authors reported that in human brain data obtained at 1.5T, apparent brain motion due to respiration was observable along the phase-encoding direction in transverse EPI series but not in the readout direction—an observation that supports susceptibility variations as a source of the phenomena (24). These effects are expected to be greater at higher magnetic field.

With these observations in mind, an important goal for the present work was to understand the effect of global respiration-induced resonance offsets on EPI image series at 7T. In addition, we focused on determining the extent to which the phenomena are dependent on sequence parameters.

THEORY

Spatial Distribution: a 3D Model

Human tissues are diamagnetic, with a magnetic susceptibility close to that of water ($\chi \approx -9.6 \times 10^{-6}$), while ambient air is paramagnetic because of the presence of oxygen ($\chi \approx +0.36 \times 10^{-6}$). Because of this ≈10-ppm difference in magnetic susceptibility, when the human

[1]Center for Magnetic Resonance Research, Department of Radiology, University of Minnesota Medical School, Minneapolis, Minnesota.
[2]Department of Radiology, Stanford University School of Medicine, Stanford, California.
Grant sponsor: National Institutes of Health; Grant numbers: RR08079; RO1MH55346; Grant sponsors: W.M. Keck Foundation; National Foundation of Functional Brain Imaging.
*Correspondence to: Pierre-François Van de Moortele, M.D., Ph.D., Center for Magnetic Resonance Research, University of Minnesota Medical School, 2021 6th Street SE, Minneapolis, MN 55455. E-mail: pfvdm@cmrr.umn.edu
Received 13 August 2001; revised 7 January 2002; accepted 8 January 2002.

body is placed in a homogenous magnetic field the resulting magnetic field is distorted in a manner that depends on the geometry and magnetic susceptibility of each compartment present in the field. During respiration, the spatial disposition of several large structures (chest walls, diaphragm, viscera, shoulders, and arms) varies continuously, leading to time-varying magnetic field distortions that can extend into the region of the brain. Computing the resulting B_0 fluctuations exactly in each location of the brain would be difficult. However, Raj et al. (18) introduced a model using an analytical approach derived from Schenk et al. (25), with an infinite cylinder of water representing the torso, and a spherical, paramagnetic gas cavity that can vary in size, position, and/or susceptibility representing the lungs and their changes during respiration.

Let the z axis be parallel to the main magnetic field B_0 and along the inferior-superior direction, while the x and y axes define a transverse plane with y along the postero-anterior direction. With Raj et al.'s model (18), the value of ΔB in the brain induced by the lungs is given by:

$$\Delta B(x, y, z) = \frac{\Delta\chi B_0 R^3}{3} \frac{[2(z-z_0)^2 - (x-x_0)^2 - (y-y_0)^2]}{[(x-x_0)^2 + (y-y_0)^2 + (z-z_0)^2]^{5/2}}, \quad [1]$$

equivalent to:

$$\Delta\nu(x, y, z) = K \frac{2(z-z_0)^2 - (x-x_0)^2 - (y-y_0)^2}{[(x-x_0)^2 + (y-y_0)^2 + (z-z_0)^2]^{5/2}}, \quad [2]$$

with

$$K = \frac{\gamma}{2\pi} \frac{\Delta\chi B_0 R^3}{3}, \quad [3]$$

where R is the radius of the sphere, (x_0, y_0, z_0) the center coordinates of the sphere, $\Delta\chi$ the susceptibility difference between the cavity and the water, and γ the gyromagnetic ratio of protons (263.57×10^6 rads^{-1} T^{-1}). The model implicitly assumes that the cylinder is parallel to the orientation of B_0. Here we utilize this model to consider respiration-induced modulations in $\Delta\nu(x, y, z)$ as a result of the variations of K with the respiratory cycle. Both lung size and oxygen gas concentration can change the value of K via changes of R and $\Delta\chi$, respectively.

The RIRO estimation in our data, $\Delta\nu_{\mathrm{RIRO}}$, is expected to reflect the differences between $K_{\mathrm{peak}} = (\gamma/2\pi)\Delta\chi_{\mathrm{peak}} B_0 R^3_{\mathrm{peak}}$ and $K_{\mathrm{low}} = (\gamma/2\pi)\Delta\chi_{\mathrm{low}} B_0 R^3_{\mathrm{low}}$, corresponding to the peak and trough of the respiration cycle, respectively. With $\Delta K_{\mathrm{RIRO}} = (K_{\mathrm{peak}} - K_{\mathrm{low}})$:

$$\Delta\nu_{\mathrm{RIRO}}(x, y, z) = \Delta K_{\mathrm{RIRO}} \frac{(2(z-z_0)^2 - (x-x_0)^2 - (y-y_0)^2)}{((x-x_0)^2 + (y-y_0)^2 + (z-z_0)^2)^{5/2}}. \quad [4]$$

This equation contains four unknowns, namely ΔK_{RIRO}, x_0, y_0, and z_0. Assuming, as suggested by Raj et al. (18), that $(x - x_0)^2 + (y - y_0)^2 \gg (z - z_0)^2$ within the imaged slab, the x and y terms can be neglected in a first approximation with:

$$\Delta\nu_{\mathrm{RIRO}}(z) = \Delta\tilde{K}_{\mathrm{RIRO}} \frac{2(z-\tilde{z}_0)^2}{((z-\tilde{z}_0)^2)^{5/2}} = \Delta\tilde{K}_{\mathrm{RIRO}} \frac{2}{(z-\tilde{z}_0)^3}. \quad [5]$$

In the following, we use $\Delta\nu$ (in Hertz) or $\Delta B_0 = 2\pi\Delta\nu/\gamma$ (in Tesla) interchangeably to refer to the RIRO amplitude. It is noted that with the 3D model, and considering that both the sphere volume and the air susceptibility are larger during the respiration peak, $\Delta\nu_{\mathrm{RIRO}}$ is always non-negative.

Sequence-Based Predictions

This study was mainly motivated by RIRO consequences in EPI fMRI series. However, it was essential in our view to confirm the RIRO phenomenon at ultra high field with various NMR sequences. Accordingly, two main categories of data were acquired, differing in the presence or absence of spatial-encoding gradients, namely free induction decays (FIDs) and multislice EPI series. In addition, a dynamic 3D fast low-angle shot (3D-FLASH) series was used to specifically address the 3D spatial accuracy of the model at higher resolution.

Single RF Pulse Experiments

FIDs acquired *without* gradients were used to first assess and quantify the amplitude of RIRO fluctuations without interference from eddy currents or other phase shifts arising from the spatial-encoding gradients. With no spatial encoding, and considering that the spatial extent of the brain tissue seen by the surface coil is small when compared with its distance to the lungs, we assumed that (as was reported at 3 Tesla (19)) the respiration-induced variations of B_0 averaged through this volume could be roughly approximated as an apparent global variation of B_0. Such a global resonance offset is easily detectable in the time domain as a linear phase shift (19,26), using the relation:

$$\Delta\Phi(\tau) = \gamma\Delta B_0\tau + \Delta\Phi_0 \quad [6]$$

where τ is the time evolved after the RF pulse, and $\Delta\Phi_0$ is a zero-order term to account for phase variations occurring mainly prior to data acquisition (eddy current, motion, hardware instability). Thus, we hypothesized that $\Delta\Phi(\tau)$ would clearly reflect RIRO phenomena.

EPI Images

In EPI images, a B_0 offset yields a linear phase shift of k-space along the phase-encoding direction, which produces a spatial shift in the image along the phase direction (21). We assumed that the respiration-induced B_0 offsets averaged through the imaged slice could be approximated as an apparent global ΔB_0 through the slice. To measure the corresponding phase evolution, the acquisition at the central point of k-space is used. As it is sampled at t = TE, its phase accumulation becomes:

$$\Delta\Phi(TE) = \gamma\Delta B_0 TE + \Delta\Phi_0, \quad [7]$$

where $\Delta\Phi_0$ is a zero-order term to account for phase variations occurring mainly prior to data acquisition. Thus, $\Delta\Phi$(TE) is expected to reflect respiration-induced fluctuations of B_0. Here it is important to take into account the slice orientation. Indeed, as shown in Eq. [5], $\Delta\nu_{RIRO}(x, y, z)$ is spatially dependent primarily on z, so it was hypothesized that the amplitude of RIRO would vary significantly with slice position along z in a transverse EPI series, increasing with slice position closer to the lungs. On the other hand, Eq. [5] also suggests that slice position along x and y, for sagittal and coronal series, should have a limited impact. To check these hypotheses, multislice EPI series were acquired along axial, sagittal, and coronal orientations.

3D-FLASH Series

To further explore the 3D spatial distribution of RIRO and compare it with the model proposed by Raj et al. (18), it was necessary to acquire images in which RIRO yielded mainly phase changes in the image domain without spatial distortions and with a reasonable spatial resolution. This was achieved by acquiring a series of 50 volumes of 3D FLASH data, and sorting the k-space lines from their location in the respiratory cycle before 3D Fourier transform (see Data Analysis). Our hypothesis was that the amplitude of the phase fluctuations correlating with the respiration cycle (calculated for each voxel) would have a 3D distribution consistent with Eq. [4].

MATERIALS AND METHODS

Subjects and Data Acquisition

Experiments were performed on a 90-cm bore magnet operating at 7 Tesla (Magnex Scientific, Abingdon, UK), driven by a Varian Inova console (Palo Alto, CA). Images were acquired with a quadrature transmit/receive surface coil positioned to cover the occipital cortex. Scout images were first obtained with an inversion-recovery-prepared TurboFLASH sequence (TI = 1.4 s, TR/TE = 8/3 ms, matrix = 128 × 128, slice thickness = 5 mm) to identify slices and voxels of interest. Adjustments of the first- and second-order shims were performed in the occipital cortex with the echo-planar version of "Fast, Automatic Shimming Technique by Mapping along projections (FASTMAP) (27). Typical linewidth of a spectrum obtained from a 40 × 40 × 40 mm^3 voxel defined by a stimulated-echo acquisition mode (STEAM) sequence was between 12 Hz and 18 Hz (0.04–0.06 ppm).

Respiration recording was performed during each series with a pneumatic belt surrounding the abdomen near the diaphragm. Respiratory activity was sampled every 10 ms and written as ASCII files (AcqKnowledge, BIOPAC Systems, Inc., CA). To align NMR data retrospectively with physiological records, a TTL signal was also recorded for each RF pulse.

Nine healthy subjects, who provided written consent, participated in this study (which was approved by the institutional review board at the University of Minnesota). For all experiments the subject was asked to remain still, with eyes closed.

Single RF Pulse Experiments

In all subjects, a series of FIDs was acquired immediately after a single RF excitation with no gradients (30μs square RF pulse, flip angle = 1° or 2.5° defined for the globally-detected signal from the surface coil, TR = 0.4 s, one series = 400 scans recorded and saved individually with no averaging). In three subjects two series were acquired. In one of these three subjects, the second series was acquired while the subject intentionally took several deep breaths.

EPI Images

In five subjects, EPI series were acquired with a gradient-recalled blipped EPI sequence in axial and sagittal orientations, as well as coronal orientation for three subjects. In each orientation, 10 slices were evenly distributed every 10 mm (or every 5 mm for one coronal series) to cover most of the brain tissue within the field of view (FOV) of the coil (FOV = 20 × 20 cm^2, matrix = 64 × 64, TE = 19 ms, TR = 2 s, interleaved odd/even slice ordering, slice thickness for axial images = 3 mm, slice thickness for sagittal and coronal images = 3 mm or 10 mm, number of scans = 150).

3D-FLASH Series

In one volunteer a series of 3D-FLASH images was continuously acquired for 10 min (50 volumes) with readout along the z axis, first phase encoding along the y axis and second phase encoding along the x axis. The corresponding matrix was 64 × 64 × 16, with FOV = 25.6 × 25.6 × 19.2 cm^3, TR/TE = 12 ms/3.7 ms, and flip angle = 10°. During the acquisition of this series, the respiratory belt signal and TTL signals from the scanner were sampled every millisecond (instead of every 10 ms) because of the shorter delay between RF pulses.

DATA ANALYSIS

Respiration Time-Course and RIRO Amplitude

To compare the amplitude of RIRO between different series, an average peak-to-peak value was derived for each time-course by regressing the B_0 fluctuations measured in the time-domain NMR data (see next two paragraphs) on a reference waveform derived from the respiration belt recording. A high correlation between the respiration belt recording and the measured B_0 fluctuations was observed in terms of both the amplitude and the temporal variation. A reference respiration waveform was generated and normalized from the respiration belt data, with an approach derived from Hu et al. (10), as follows. After polynomial detrending to remove long-term drifts, the maximum peak of each respiration cycle was detected along the respiration time-course. Then the fractional value of respiration cycle, ranging between 0 and 1, was evenly distributed among respiration sampling times within each respiration cycle. After this temporal resampling, the resulting respiration time-course was fitted with a series of sinusoidal curves using a least-squares method. The resulting respiration reference waveform was normalized, scaling from 0 to 1, and used as a regressor to perform a multiple regression with B_0 fluctuation time-course (the second re-

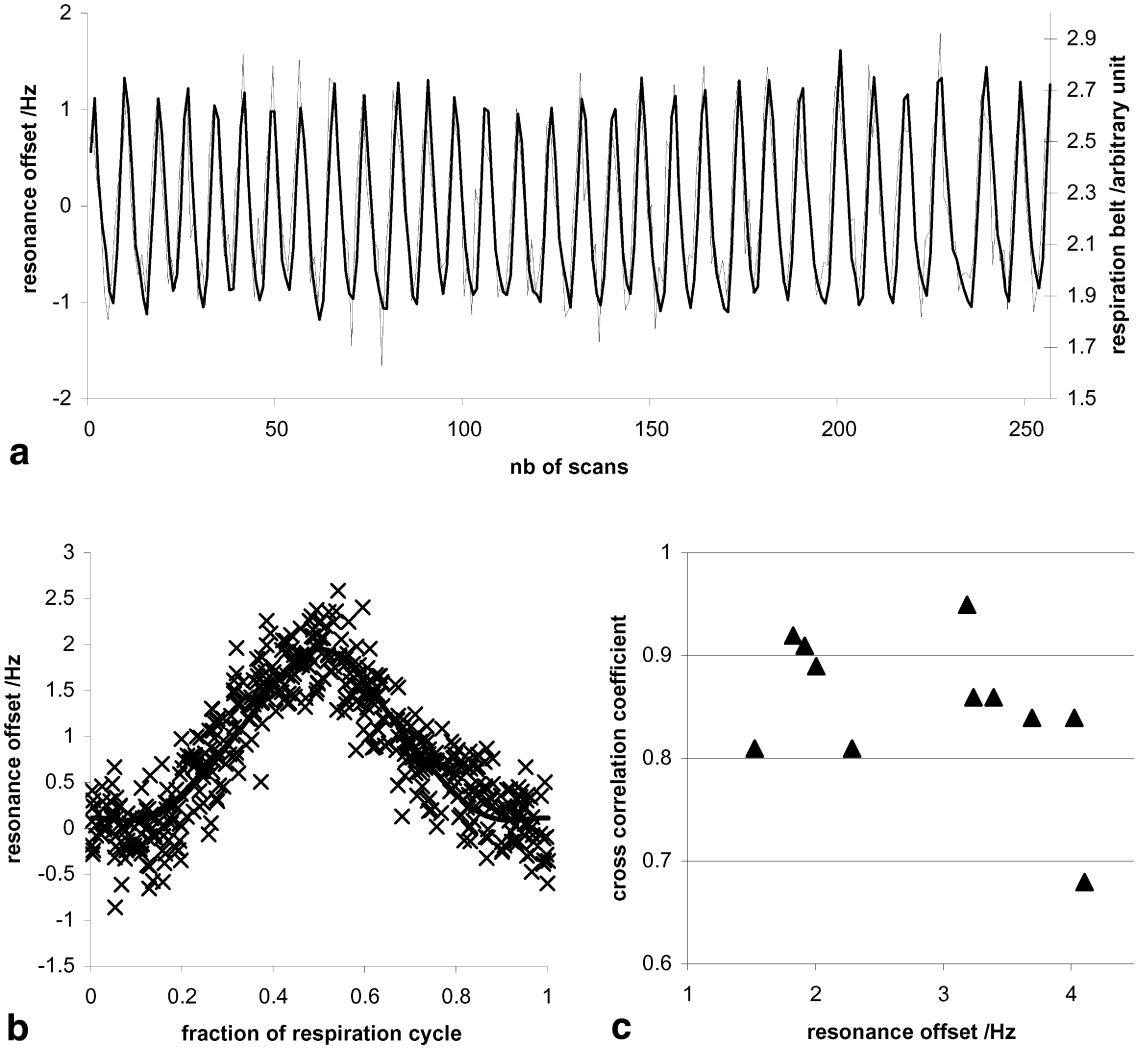

FIG. 1. **a:** Typical time-courses obtained from one subject during the FID experiment. Thick line: plethysmographic respiration belt record. Thin line: resonance offset calculated for each FID recorded after an RF pulse without gradient. The two curves present very comparable modulations in shape and amplitude (curves are centered on resonance axis origin). **b:** Resonance offsets (crosses) measured along the whole series plotted as a function of fraction in the respiratory cycle. The reference waveform calculated from respiratory data (see text) is overplotted (plain line) as a function of fraction in the respiratory cycle (minimum of waveform is set to resonance axis origin). **c:** Cross-correlation between respiration belt record and respiration-induced B_0 fluctuation as a function of average peak-to-peak respiration-induced resonance offset. FIDs were obtained after a single RF pulse without gradient. The average cross-correlation coefficient is 0.84 SD = 0.07), with only one value below 0.8 among 11 measured series. No significant relation was found between RIRO amplitude and cross-correlation coefficient.

gressor being a constant factor). The regression coefficient calculated for the waveform regressor was used as an estimate of the average peak-to-peak RIRO amplitude for each series. The cross-correlation coefficient between the respiration belt recording and the B_0 fluctuation time-course was also computed.

Apparent B_0 Time-Course in Single RF Pulse Experiments (FIDs)

For FIDs acquired *without* gradients, the phase of each complex data vector was unwrapped to remove $+/-\pi$ jumps. One scan in a series was taken as a reference from which the phase of the corresponding sample of all other scans of the series was subtracted. For each resultant phase difference vector (one per scan), the apparent B_0 offset was calculated as the slope of a least-squares linear fit between phase difference $\Delta\Phi(\tau)$ and sampling time (τ) , using Eq. [6]. Only the first 10 ms of the FIDs were used for least-squares fitting. A polynomial detrending was performed on the resulting B_0 time-course to remove the long-term drifts and thus focus on respiration-related fluctuations. Then RIRO amplitude was computed as described in the previous paragraph.

Apparent B_0 Time-Course in EPI Series

For EPI images, the phase of the central point of the *k*-space (defined as the maximum modulus intensity point) was used together with its acquisition time (TE) to calculate the apparent B_0 fluctuation. We noticed from numerous other acquisitions (data not shown) that the zero-order phase term $\Delta\Phi_0$ in Eq. [7] was negligible. Thus, Eq. [7] was simplified into:

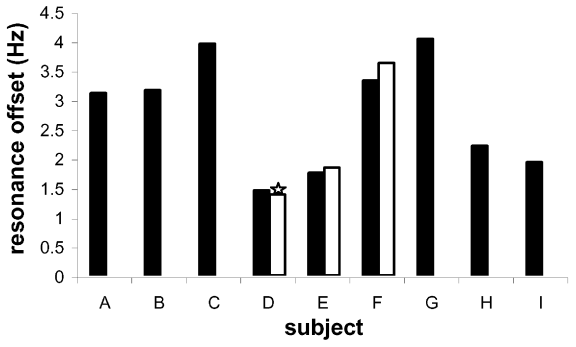

FIG. 2. Average peak-to-peak RIRO amplitude measured in single RF pulse series for nine subjects (dark bars). Note the high inter-subject variability. For three subjects (D, E, and F) the series was run a second time (white bars). Volunteer D was asked, during the second series (marked with a star), to make a few big breaths, which did not change the RIRO amplitude estimation, although the SD of the B_0 fluctuation was multiplied by 6.

$$\Delta\Phi(TE) = \gamma\Delta B_0 TE + \Delta\Phi_0 \approx \gamma\Delta B_0 TE \quad (\text{with } \Delta\Phi_0 \approx 0), \qquad [8]$$

from which ΔB_0 can be derived. The position for the *k*-space center, based on maximum intensity of the echo signal, was determined slice by slice for each time series. The resulting B_0 time-courses were detrended before computing RIRO amplitude as described above.

3D-FLASH Series

For the 3D-FLASH series, the first 10 volumes were eliminated to account for the approach to the steady state as well as to exclude one big breath observed on the respiration belt time-course. The respiration cycle amplitude did not vary significantly for the remainder of the series. The respiratory belt time-course was analyzed as described above to evaluate the fractional value of the respiration cycle at each RF pulse. Then, each line of the 3D *k*-space was sorted depending on its fractional value. To obtain a 3D map of RIRO amplitude, we prepared two 3D *k*-space data sets: one with *k*-space lines sampled closest to the peak of respiration cycles, the other with *k*-space lines sampled closest to the trough of respiration cycles. Each of the 3D *k*-space data sets was 3D Fourier transformed, and the two corresponding 3D complex images were divided voxel by voxel (only voxels passing a signal-to-noise threshold were considered). The phase $\Delta\Phi(x, y, z)$ of the resulting 3D complex ratio was used to estimate $\Delta\nu_{\text{RIRO}} = \Delta\Phi(x, y, z)/TE$ with TE = 3.7 ms, which in turn was fitted with the 3D model using Eq. [4].

One-dimensional projections of $\Delta\nu_{\text{RIRO}}$ were computed along the *z*, *y*, and *x* axes by averaging $\Delta\nu_{\text{RIRO}}$ along the *yx*, *zy*, and *zy* planes, respectively, yielding $\Delta\nu_{\text{RIRO}YX}(z)$, $\Delta\nu_{\text{RIRO}ZX}(y)$, and $\Delta\nu_{\text{RIRO}ZY}(x)$, allowing a summarized view of the data. The residuals, $\Delta\nu\text{res}_{\text{RIRO}}(x, y, z)$, obtained by subtracting the fitted model from the data, were also averaged along the three axes, yielding $\Delta\nu\text{res}_{\text{RIRO}YX}(z)$, $\Delta\nu\text{res}_{\text{RIRO}ZX}(y)$, and $\Delta\nu\text{res}_{\text{RIRO}ZY}(x)$.

RESULTS AND DISCUSSION

Single RF Pulse Experiments

RIRO in single-pulse FIDs was clearly detected in all experiments, with a remarkable correspondence between the respiration belt recording and the estimated B_0 fluctuation. The average correlation coefficient value between the two time-courses was 0.84 SD = 0.07). This cross-correlation coefficient did not show a statistically significant dependence on RIRO amplitude, indicating that the measurement was not SNR-limited. Figure 1 shows representative results obtained with the one pulse experiment and the corresponding reference respiration waveform. As shown in Fig. 2, the overall variability of RIRO amplitude among subjects was quite high, ranging from 1.45 Hz to 4 Hz, suggesting that differences in anatomy as well as in respiration represent a main factor affecting the RIRO amplitude.

In general, the respiratory patterns as measured by the respiration belt tended to be subject-specific: some volunteers breathed at a constant rate and amplitude, while others had low-frequency modulations in both amplitude and cycle duration. Overall, all subjects exhibited at least a few spontaneous deep breaths during a complete study, with corresponding RIRO amplitude jumps reaching 4–10 Hz. This means that respiration can account for periodic, partially periodic fluctuations, and isolated noise peaks in signal time-courses if the acquisition is frequency-sensitive. Consistent with the subject variation observed, the power spectra of both the respiration record and RIRO time-courses showed very sharp peaks at the respiration frequency for some subjects, in contrast to much broader peaks for other subjects (data not shown). This suggests

Table 1
Regression Analysis of Average RIRO as a Function of Slice Position in Multi-slice EPI Series in Three Different Orientations

Orientation	Transverse			Sagittal			Coronal		
	r^2	Slope (Hz/cm)	(SE)	r^2	Slope (Hz/cm)	(SE)	r^2	Slope (Hz/cm)	(SE)
Subject 1	0.935*	−0.160	0.015	0.357	−0.035	0.017	nd	nd	nd
Subject 2	0.978*	−0.374	0.020	0.073	0.025	0.031	nd	nd	nd
Subject 3[a]	0.992*	−0.380	0.012	0.000	0.000	0.043	0.019	−0.032	0.081
Subject 4	0.938*	−0.155	0.014	0.055	−0.017	0.024	0.620**	−0.093	0.026
Subject 5	0.911*	−0.287	0.032	0.006	0.008	0.024	0.196	−0.088	0.063

Origin of slice position axis was arbitrarily set at the center of the imaged slab in all orientations.
[a]See also Fig. 3 for results obtained in Subject 3.
*$P < 10^{-4}$; **$P < 10^{-2}$; r^2 values are without mark for $P > 0.05$; nd, no data; SE, standard error of slope (Hz/cm).

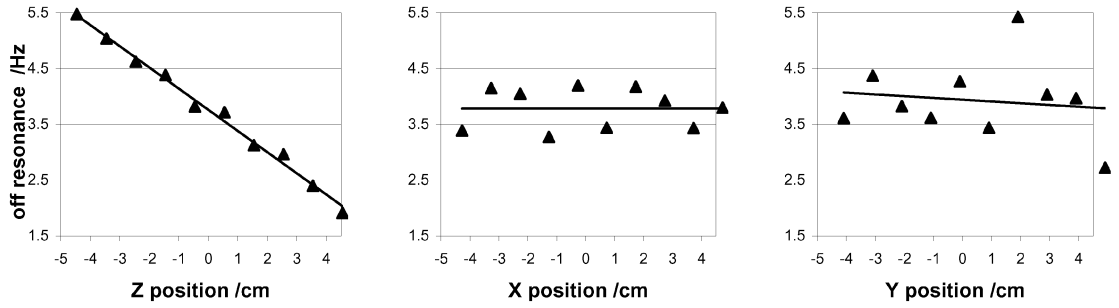

FIG. 3. Average peak-to-peak amplitude of respiration-induced resonance offset for one volunteer in three orientations in multislice EPI as a function of slice position. Axis origins for slice position along the *z*, *x*, and *y* axes in the axial, sagittal, and coronal series, respectively, are arbitrarily defined as the center of each imaged slab. Slices are 1 cm apart. Slice position increases along a foot-to-head direction in the transverse series, along a left-to-right direction in the sagittal series, and along a posterior-to-anterior direction in the coronal series. On each chart a linear fit is overplotted (straight line). Note the linear relationship observed in the axial series as opposed to the sagittal and coronal series (see also Table 1; data shown here were obtained in subject 3).

that data-correction approaches based on spectral filtering have to match those individual characteristics (15,17).

In the repeated acquisitions (three volunteers), the RIRO amplitude was reproducible. For the scan in which the volunteer was asked to take a few big breaths, the peak-to-peak RIRO reached 14 Hz, while the average estimation used in this study did not significantly change, as can be seen in Fig. 2. Visual inspection of the respiration belt data confirmed that, apart from the few very big breaths, the respiration amplitude was similar within the two series. This observation shows that the average peak-to-peak RIRO amplitude estimated in this study, based on the regression of B_0 time-course on the reference respiratory waveform, is robust against occasional large variations in respiration. In contrast, the few high peaks present in the second one-pulse series were sufficient to increase the global SD of the corresponding B_0 time-course by sixfold.

Multislice EPI Series

In all EPI series, RIRO was clearly detected on a slice-by-slice basis, with a peak-to-peak amplitude ranging from 0.7 Hz to 5.4 Hz. The most striking feature was the impact of the slice orientation on the slice position dependence. In the axial series, there was a very high correlation between average peak-to-peak RIRO amplitude and slice position for the five volunteers, with the value of RIRO increasing along the cranial-caudal direction. As shown in Table 1, this high correlation was observed in all subjects. Representative curves obtained for one volunteer can be seen in Fig. 3. However, in the sagittal orientation there was no significant correlation between position along the *x* axis and RIRO amplitude. In coronal orientation, a significant correlation between RIRO amplitude and slice position along the *y* axis was found in only one volunteer, with $r^2 = 0.62$ (to be compared with $r^2 > 0.91$ in the axial series). This could reflect center-of-mass (along the *z* axis) changes between different coronal slices (along the *y* axis), which in turn would affect the corresponding average RIRO amplitude according to the dependence along *z* that we report.

The predominant effect in the *z* direction points strongly towards a susceptibility modulation associated with the lung volume as the source of the phenomenon. Interestingly, an empirical coefficient of $\sim 1/10\ \text{cm}^{-1}$ was observed in all subjects between the rate of RIRO decrease per centimeter and the value of RIRO amplitude averaged through the imaged slab, as shown in Table 2. This intersubject invariance is likely because the relevant geometry is approximately subject-invariant. This is in contrast to the difference in RIRO amplitude between the inferior and superior transverse slices (10-cm slab), ranging from 1.4 Hz to 3.6 Hz, which emphasizes again the substantial degree of intersubject variation.

The model proposed by Raj et al. (18) shows that EPI images are expected to be not only shifted along the phase-encoding direction but also distorted and exhibiting intensity-profile alteration. However, we studied here mainly

Table 2
Coefficient Obtained by Dividing the Slope of RIRO Decrease Along the *Z* Axis by the RIRO Value Averaged Through Imaged Slab in Transverse Multi-slice EPI Series

	RIRO slope (Hz.cm^{-1})	Average RIRO (Hz)	Coefficient, slope/average (cm^{-1})	Regression analysis		
				Mean coefficient (±SE)	Intercept (±SE)	r^2
Subject 1	0.160	1.658	0.097			
Subject 2	0.374	3.561	0.105			
Subject 3	0.380	3.704	0.103	0.106 (±0.009)	0.006 (±0.029)	0.959*
Subject 4	0.155	1.460	0.106			
Subject 5	0.287	2.389	0.120			

SE, standard error; *$P < 5 \times 10^{-3}$.

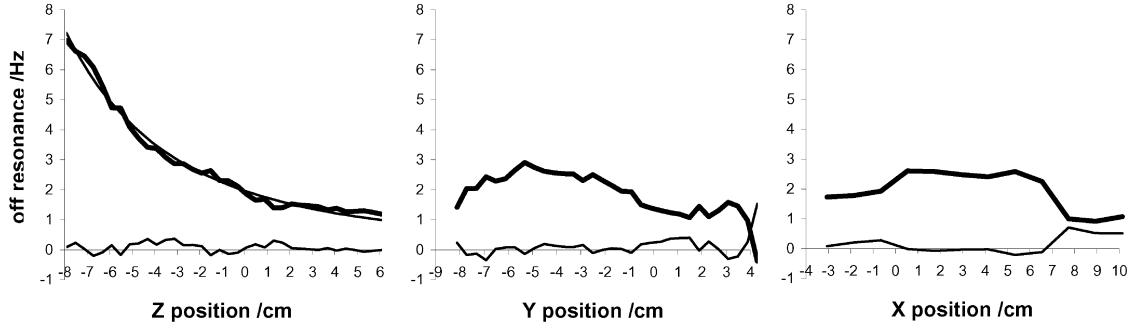

FIG. 4. Projection along the *z*, *x*, and *y* axes of averaged respiration-induced resonance offset (thick line), $\Delta\nu_{RIROYX}(z)$, $\Delta\nu_{RIROZX}(y)$, and $\Delta\nu_{RIROZY}(x)$, respectively, as well as the corresponding averaged residuals (lower thin line) after fitting the data with Eq. [4] (see Data Analysis). $\Delta\nu_{RIRO}(x, y, z)$ and $\Delta\nu res_{RIRO}(x, y, z)$ were averaged along the *yx*, *zx*, and *zy* planes. For the *z* axis the fit (upper thin line) obtained for $\Delta\nu_{RIROYX}(z)$ with Eq. [5] (see Data Analysis) is also overplotted. Axes are oriented along a foot-to-head direction for *z*, posterior-to-anterior for *y*, and left-to-right for *x*. Axis origins are set at the isocenter of the gradient coil. Note the predominant dependence of RIRO amplitude on the *z* direction as opposed to the *x* and *y* directions.

the issue of global phase alteration in the time domain, the linear component of which translated into image shifts. Rather than measuring the center of mass in EPI images, we utilized the phase of the *k*-space center, as already reported (22). We found this approach to be significantly more sensitive, particularly for slices near the edges of the FOV of our surface coil, where the total amount of signal is low. This approach was also less demanding in terms of computing time, and avoided potential interference with residual Nyquist ghosting in the image domain, as well as thresholding and/or masking issues.

The prominent *z* dependence of RIRO amplitude has important implications. It suggests that in EPI fMRI series the residual variance may be higher in the inferior part of the brain, leading to a concomitantly lower activation detectability if no correction is used. At 7T this is not a negligible effect: in fMRI experiments, typical EPI parameters have a sampling bandwidth along the phase-encoding direction ranging between 15 and 30 Hz/pixel. A 5-Hz peak-to-peak RIRO effect means a corresponding shift in EPI images as large as one-sixth to one-third of a pixel. The spatial distribution along *z* also indicates that if one aims at correcting EPI series for respiration-induced, off-resonance artifacts, a simple model suffices for transverse EPI acquisitions, assuming that a linear phase shift in the time domain explains the largest part of respiration-induced phase disturbance (28). For images acquired along coronal or sagittal orientations, a simple linear phase shift approximation may not be sufficient.

3D-FLASH Series

In the 3D data set, a high dependence of RIRO amplitude on *z* is easily seen in 1D projections of phase data along the three axes, as shown in Fig. 4. In addition, it can be seen that $\Delta\nu_{RIROYX}(z)$ varies nonlinearly with *z*, a feature detectable in 3D FLASH data because of the larger extent of tissue coverage along *z* compared to EPI experiments. Data projection on the *z* axis fitted nicely with the simplified model from Eq. [5]. As for the EPI series, $\Delta\nu_{RIRO}$ variation was more substantial along *z* than along *y* and *x*, a feature predicted by Raj et al.'s model assuming $(x - x_0)^2 + (y - y_0)^2 \gg (z - z_0)^2$. The apparent linear relationship between RIRO and the *z* position in the transverse EPI series was an acceptable approximation for the limited extent of imaged tissue, which, in addition, was not as close to the lung as the lower part of the imaged tissue in the FLASH series. When fitting the 3D data with Eq. [4], the model proved to account for most of the correlation. This can be seen in Fig. 4, with the residuals along *z*, *y,* and *x* close to zero.

A small fraction of the data did not behave according to those global observations, with some higher values of the residuals along *x* and *y*, respectively for $y = 4$ cm and $x = 7–9$ cm. However, this corresponds to a limited number of voxels located in the very anterior and lateral parts of the imaged tissue, which is close to the limits of the coil coverage, where the SNR was marginal. Nevertheless, the model clearly captured the main features in the measured phase variation, leaving only random noise in the residual that is distributed approximately with a Gaussian distribution, as shown in Fig. 5. A linear regression of Δ_{RIRO} on the fitted 3D model proved statistically highly significant with $F = 6537$ and $P < 10^{-6}$.

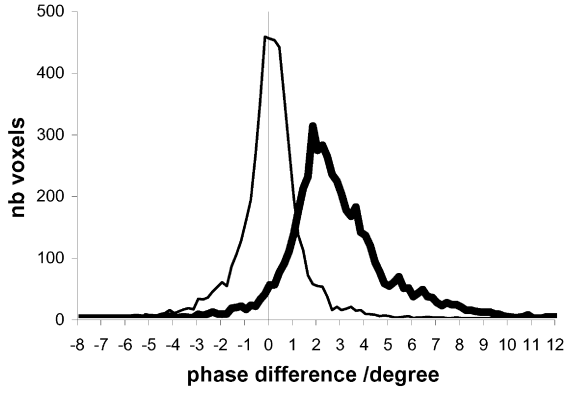

FIG. 5. Distribution of phase difference (thick line) between peak and trough of respiration cycle $\Delta\Phi(x, y, z) = \Delta\nu_{RIRO}(x, y, z) \cdot TE/360$, expressed in degrees, and of its residuals $\Delta\Phi(x, y, z) = \Delta\nu_{RIRO}(x, y, z) \cdot TE/360$, (thin line) after fitting the data with Eq. [4] (see Data Analysis). Distributions were computed with a bin size of 0.2°. Total number of voxels is 4970. Mean (±SD) for $\Delta\Phi(x, y, z)$ and its residual $\Delta\Phi res\ (x, y, z)$ were 2.12° (±1.56) and 0.00° (± 1.36), respectively.

Another interesting number from the fit was the estimated coordinates of the center of the sphere modeling the lungs, for which it was found $z_0 = -23$ cm, $y_0 = -7$ cm, and $x_0 = -1$. For x_0 and y_0 those values are possible: x_0 is indeed expected to be close to the x origin of the gradient coil, as it is close to the plane of anatomic symmetry; y_0 is expected to be dependent on relative positions of both the head and the chest along y. The value found here could be inside such limits, but systematic measure of the volunteer's chest within the magnet with a given set of mattress, foam, and coil was not performed. On the other hand, z_0 was not in the range of an acceptable value for the center of the lungs; rather, it corresponded to their apex. However, the sphere model is clearly a rough approximation to the true, complex physiology of the body. Indeed, when going "close to the source," the true spatial distribution of different susceptibility materials is of critical importance to determine the local values of ΔB_0. This work was dedicated to RIRO detection in the brain only, and it is speculated that in a larger population the RIRO amplitude will be found with a similar functional shape along z, and with a subject-specific scaling factor.

All data presented here were acquired in the occipital lobe with a surface coil. Further exploration of other brain areas will help to complete a global description of the 3D spatial distribution of respiration-induced resonance offset at very high field.

CONCLUSIONS

Respiration-induced B_0 fluctuations in the human brain were investigated at 7 Tesla in the occipital lobe with single RF pulse series, multislice EPI series, and a 3D FLASH dynamic series. Several important features were demonstrated: 1) RIRO was clearly detectable in all data sets, and proved to be mainly a susceptibility-induced phenomenon. 2) A high correlation existed between RIRO and the pneumatic respiration belt recording. 3) The global peak-to-peak amplitude of respiration-induced resonance offset was highly dependent on subjects and ranged from 1.45 Hz to 4 Hz. 4) The amplitude of RIRO varied monotonically with the axial position in axial multislice EPI over a 10-cm slab, reaching up to 5.4 Hz in the lowest slice. 5) For the 3D FLASH data, the analytical model published by Raj et al. (18) proved to describe the experimentally-detected RIRO spatial distribution accurately. This study also indicated that the slice orientation has a strong impact on respiration-induced artifacts in EPI acquisitions.

ACKNOWLEDGMENTS

We thank Gregor Adriany for the coil design, Helmut Merkle and Peter Andersen for hardware support, and Rolf Gruetter and Ivan Tkac for the FAST(EST) MAP.

REFERENCES

1. Ugurbil K, Hu X, Chen W, Zhu XH, Kim S-G, Georgopoulos A. Functional mapping in the human brain using high magnetic fields. Phil Trans R Soc Lond B 1999;354:1195–1213.
2. Yacoub E, Shmuel A, Pfeuffer J, Van de Moortele PF, Adriany G, Andersen P, Vaughan JT, Merkle H, Ugurbil K, Hu X. Imaging brain function in humans at 7 Tesla. Magn Reson Med 2001;45:588–594.
3. Tkac I, Andersen P, Adriany G, Merkle H, Ugurbil K, Gruetter R. In vivo 1H NMR spectroscopy of the human brain at 7 T. Magn Reson Med press2001;46:451–456.
4. Vaughan JT, Garwood M, Collins CM, Liu W, DelaBarre L, Adriany G, Andersen P, Merkle H, Goebel R, Smith MB, Ugurbil K. 7T vs. 4T: RF power, homogeneity, and signal-to-noise comparison in head images. Magn Reson Med 2001;46:24–30.
5. Weisskoff RM, Baker J, Belliveau J, Davis TL, Kwong KK, Cohen MS, Rosen BR. Power spectrum analysis of functional-weighted MR data: What's in the noise? In: Proceedings of the 12th Annual Meeting of SMRM, New York, 1993. p 7.
6. Jezzard P, LeBihan D, Cuenod C, Pannier L, Prinster A, Turner R. An investigation of the contribution of physiological noise in human functional MRI studies at 1.5 Tesla and 4 Tesla. In: Proceedings of the 12th Annual Meeting of SMRM, New York, 1993. p 1392.
7. Noll DC, Schneider W. Respiration artifacts in functional brain imaging: sources of signal variation and compensation strategies. In: Proceedings of the 2nd Annual Meeting of SMRM, San Francisco, 1994. p 647.
8. Noll DC, Schneider W. Theory, stimulation, and compensation of physiological motion artifacts in functional MRI. In: Proceedings of the 1st IEEE Conference on Image Processing, Austin, 1994. p 40–44.
9. Hu X, Kim S-G. Reduction of physiological noise in functional MRI using navigator echo. Magn Reson Med 1994;31:495–503.
10. Hu X, Le TH, Parrish T, Erhard P. Retrospective estimation and compensation of physiological fluctuation in functional MRI. Magn Reson Med 1995;34:210–221.
11. Le TH, Hu X. Retrospective estimation and correction of physiological artifacts in fMRI. Magn Reson Med 1996;35:290–298.
12. Wowk B, McIntyre MC, Saunders JK. k-Space detection and correction of physiological artifacts in fMRI. Magn Reson Med 1997;38:1029–1034.
13. Frank LR, Buxton RB, Wong EC. Estimation of respiration-induced noise fluctuations from undersampled multi-slice fMRI Data. Magn Reson Med 2001;45:635–644.
14. Noll DC, Genovese CR, Vazquez AL, O'Brien JL, Eddy WF. Evaluation of respiratory artifact correction techniques in multishot spiral. Magn Reson Med 1998;40:633–639.
15. Buonocore MH, Maddock RJ. Noise suppression digital filter for functional magnetic resonance imaging. Magn Reson Med 1997;38:456–469.
16. Glover GH, Li TQ, Ress D. Image-based method for retrospective correction of physiological motion. Magn Reson Med 2000;44:162–167.
17. Chuang K-H, Chen J-H. IMPACT: image-based physiological artifacts estimation and correction technique for functional MRI. Magn Reson Med 2001;46:344–353.
18. Raj D, Paley DP, Anderson AW, Kennan RP, Gore JC. A model for susceptibility artefacts from respiration in functional echo-planar magnetic resonance imaging. Phys Med Biol 2000;45:3809–3820.
19. Henry PG, Van de Moortele PF, Giacomini E, Nauerth A. Field-frequency locked in vivo proton MRS on a whole-body spectrometer. Magn Reson Med 1999;42:636–642.
20. Jezzard P, Balaban RS. Correction for geometric distortion in echo planar images from B_0 field variations. Magn Reson Med 1995;34:65–73.
21. Jezzard P, Barnett AS, Pierpaoli C. Characterization of and correction for eddy current artifacts in echo planar. Magn Reson Med 1998;39:801–812.
22. Durand E, Van de Moortele P-F, Pachot-Clouard M, Le Bihan D. Artifact due to B_0 fluctuations in fMRI: correction using the k-space central line. Magn Reson Med 2001;46:198–201.
23. Jezzard P. Effects of B_0 magnetic drift on echo planar functional magnetic resonance imaging. In: Proceedings of the 4th Annual Meeeting of ISMRM, New York, 1996. p 1817.
24. Raj D, Paley D, Anderson AW, Kennan RP, Gore JC. Respiratory effects in functional magnetic resonance imaging due to bulk susceptibility changes. In: Proceedings of the 9th Annual Meeting of ISMRM, Glasgow, Scotland, 2001. p 67.
25. Schenck JF. The role of magnetic susceptibility in magnetic resonance imaging: MRI magnetic compatibility of the first and the second kinds. Med Phys 1996;23:815–850.
26. Bracewell RN. The Fourier transform and its applications. New York. McGraw-Hill International Editions; 1986. 474 p.
27. Gruetter R, Tkac I. Field mapping without reference scan using asymmetric echo-planar techniques. Magn Reson Med 2000;43:319–323.
28. Pfeuffer J, Van de Moortele P-F, Ugurbil K, Hu X, Glover G. Correction of physiologically-induced global off-resonance in dynamic echo-planar and spiral functional imaging. Magn Reson Med 2002;47:344–353.